Electric Power Systems Research 226 (2024) 109938

Contents lists available at ScienceDirect

Electric Power Systems Research

journal homepage: www.elsevier.com/locate/epsr

Fault-tolerant control for a microgrid with PV systems and energy storage systems integrated into quasi-Z-source cascaded H-bridge multilevel inverter

Pablo Horrillo-Quintero [a], Pablo García-Triviño [a], Raúl Sarrias-Mena [b], Carlos A. García-Vázquez [a], Luis M. Fernández-Ramírez [a,*]

[a] Research Group in Sustainable and Renewable Electrical Technologies (PAIDI-TEP023), Department of Electrical Engineering, Higher Technical School of Engineering of Algeciras (ETSIA), University of Cádiz, Avda. Ramón Puyol, s/n. 11202 Algeciras (Cádiz), Spain
[b] Research Group in Sustainable and Renewable Electrical Technologies (PAIDI-TEP023), Department of Engineering in Automation, Electronics and Computer Architecture & Networks, Higher Technical School of Engineering of Algeciras (ETSIA), University of Cádiz, Avda. Ramón Puyol, s/n. 11202 Algeciras (Cádiz), Spain

ARTICLE INFO

Keywords:
Microgrid
Fault-tolerant operation
Quasi-Z-source cascaded H-bridge multilevel inverter
Photovoltaic power plant
Energy management system

ABSTRACT

To ensure the reliability of microgrids (MGs), this paper presents a multi-fault tolerant control for a three-phase energy storage quasi-impedance multilevel-cascaded H-bridge inverter (ES-qZS-CHBMLI) with a photovoltaic (PV) power generation-based MG. In this paper, a battery energy storage system (BESS) is implemented to smooth out the PV generation fluctuations. In the event of a fault, most studies propose the injection of a fundamental zero sequence (FZS) to balance the system after a fault. However, the FZS based-method increases the modulation and it is limited by the converter operation range. The state-of-charge (SOC) unbalanced problem has traditionally been solved by balancing the BESSs as a single unit. This paper introduces an energy management system (EMS) based on the SOC proportional power distribution to balance the power injected into the grid. When one bridge faults, it is bypassed, and the remaining bridges in that phase change their operating conditions according to the references set by the EMS. Individual phase control allows multi-fault issues to be addressed. The simulation results of a three-phase grid-connected ES-qZS-CHBMLI PV-based MG implemented in MATLAB/Simulink validate the proposed multi-fault control and EMS. In addition, an experimental validation (based on OPAL RT4520 and dSPACE MicroLabBox units) confirm these results.

1. Introduction

1.1. Background

The continuous increase in RETs to power markets is a technical, environmental and economic challenge that requires major research efforts [1]. Among the current technologies, PV solar energy is one of the most implemented technologies, with a power capacity of approximately 1 TW worldwide [2]. The rapid advancement of solar cells and declining costs have contributed to an increase in grid-connected PV power systems [3]. Typical PV power system configurations perform energy conversion in two stages. Because the output voltage of PV panels is generally low, a boost converter DC/DC is usually implemented to fulfill grid demands and perform the maximum power point tracking (MPPT) strategy. However, the grid requires an AC supply, and therefore, a voltage source inverter (VSI) is employed to perform DC/AC conversion.

Currently, new inverter topologies based on impedance networks offer interesting advantages over traditional VSI. Impedance source inverter (ZSI) or quasi-impedance source inverter (qZSI) present an impedance network at the DC side of the inverter. This impedance structure allows to increment the output PV voltage, removing the DC/DC converter.

Moreover, this configuration avoids filtering components and the switching ripple is also reduced. In contrast to the VSI, the voltage gain is higher for the qZSI and performs the energy conversion in a single stage. Furthermore, qZSI configuration presents the advantage of obtaining a constant direct current from the PV generator, instead of the pulsating current obtained in the case of ZSI [4].

Grouping several converters makes it possible to respond to elevated

* Corresponding author.
E-mail address: luis.fernandez@uca.es (L.M. Fernández-Ramírez).

https://doi.org/10.1016/j.epsr.2023.109938
Received 4 July 2023; Received in revised form 25 September 2023; Accepted 10 October 2023
Available online 14 October 2023

power requirements [5]. The most commonly employed multilevel converter topologies are cascaded H Bridge (CHB), flying capacitor and neutral point clamp. New topologies use a bypass diode technique to achieve a low total harmonic distortion (THD) [6].The CHB topology provides an individual MPPT strategy for each PV power plant that is connected to each inverter. In addition, the modular configuration allows to increase the rated power of the system adding modules in series. The reduced THD and fault tolerance improve power quality, flexibility, and reliability [7]. The authors of [8] proposed a new topology for a three-phase multilevel inverter with a low THD for PV systems with different ratings. In [9], a comprehensive study of symmetric and asymmetric multilevel inverters was proposed for Electric Vehicles (EVs) applications. The results confirmed that, for a few modules, a symmetric topology provides fewer distortions than an asymmetric topology.

1.2. Challenges

In the event of non-uniform irradiation, dust on the surface of the panel, or faults in the converters, the system has the drawback of unbalanced power generation and the injection of unbalanced current into the local grid. According to [10], the unbalanced power generation is divided as: (1) phase-to-phase (bundled) power unbalance, which happens when the power delivered by each phase is dissimilar; and (2) bridge-to-bridge (individual) power unbalance, which occurs when each bridge provides different powers in the same phase. Improving the reliability of renewable systems under power converter failures is one of the main issues that need to be addressed.

1.3. Literature review

Different strategies have been proposed to control PV power systems under different failure scenarios. The authors of [11] proposed a bypass solution for a single-bridge fault. When one bridge faults, one healthy bridge is eliminated in the remaining phases to compensate the power generation, wasting the power that these converters can deliver to the grid. Feed-forward control was introduced in [12] for single-phase systems and in [13] for three-phase, to solve inter-bridge power imbalanced. A fundamental zero frequency sequence (FZS) is commonly added to shift the neutral point [14]. The target of neutral-point-shifted is to distribute the power from the healthy phases to the phase where the fault occurs. However, zero-sequence injection increases the output voltage of the inverter, which can lead to overmodulation of the H-bridge in case of a severe power unbalance. Reference [15] introduced an optimal zero sequence injection for a CHB in order to extend the power balance range, and a simplified zero sequence injection, but added negative sequence grid current. A robust three-phase solar PV fed fault-tolerant CHB inverter was presented in [16], where the faulty cell was isolated, and the control scheme maintained the converter output voltage. In [17], a fault-tolerant scheme based on fundamental phase shift compensation PWM (FSC-PWM) was presented. This modulation technique is based on phase shifts of the carrier signals, providing balanced line voltages. An improvement in the post-fault performance of CHB was studied in [18], which decreased the common-mode voltage when the output voltage was attenuated. The authors of [19] proposed a control structure to improve the dynamic performance of a Modular Multilevel Converter under pole-to-pole DC faults in a high-voltage direct current system (HVDC). A new topology for a CHB multilevel inverter was proposed in [20] to compensate for open-circuit faults by increasing the output voltage level. The aforementioned works developed control algorithms for failure situations and diagnosis techniques. Besides, other optimization techniques have been proposed to mitigate the effects of failure. The authors of [21] used an intelligent neural network to diagnose, detect, and monitor faults in a PV power system.

It is common to accompany a renewable generation source with an energy storage system (ESS) to smooth out renewable power fluctuations, thereby improving the reliability of the system [22]. Typically, MGs are supplemented with Li-ion batteries owing to their high efficiency and long service life [23]. Nevertheless, it is necessary to develop an energy management system (EMS) that coordinates the power exchange between renewable energy sources and ESSs. Reference [24] presented for a battery energy storage system (BESS) a fault-tolerant control based on a multilevel cascade PWM converters. The aim of the control system is to share an equal amount of power between phases after a fault. Therefore, each BESS has the same stage of charge (SOC) in each phase. Balancing control for a multilevel inverter with cascaded H-bridge topology and energy storage (ES-CHBMLI) and fault-tolerant operation have also been studied for electric vehicle (EV) applications [25]. A comprehensive review of SOC balancing methods in multilevel converters-based BESS was carried out in [26] for single and multi-phase systems. In the case of single-phase configurations, only submodule SOC balancing is carried out, whereas in three-phase CHBMLI a FZS injection is typically used for phase SOC balancing as well as submodule SOC balancing. In [27], a generalized analytic solution to the unbalanced power distribution among CHB modules with BESSs was presented. A simplified control method for large multilevel converters was demonstrated. In the case of hybrid energy storage system (HESS), [28] introduced a new cascaded multilevel converter topology in which an LC branch controls the harmonic frequency component in the power distribution between HESS. Reference [29] presented a power-matching algorithm for SOC balancing control. The proposed method guarantees the balancing speed without zero detection circuit and low switching losses. In off-grid applications [30], a simplified multilevel space vector pulse width modulation (SVPWM) was selected for SOC balancing. The results depicted an improvement in the voltage waveform, distortion and efficiency.

1.4. Scope

The combination of BESSs and CHBMLI (ES-CHBMLI)-based PV power plants has been studied in the literature [31]. Reference [32] introduced an ES-qZS-CHBMLI for a single-phase grid-connected system. The proposed control scheme allowed effective control under different irradiation conditions. A simplified model of an ES-qZS-CHBMLI presented in [33] demonstrated an adequate dynamic of the converter with low computational requirements to meet the grid requirements and economic dispatch of storage energy. These papers demonstrate the effectiveness of the ES-qZS-CHBMLI under normal operation. One of the main advantages of the ES-qZS-CHBMLIs is their reliability owing to modular structure and the use of shoot-through state, which reduces the chance of catastrophic failure. However, there is a research gap in the study of ES-qZS-CHBMLI under fault operations.

Most authors suggest a FZS injection [10]. The FZS technique requires increasing the inverter output voltage, which implies overmodulation of the converter and redistributing power from the healthy phases to the phase where the fault is occurring. Therefore, there is a physical limitation on the maximum voltage to be withstood at the inverter output, which implies a limit on the number of faults that the system can withstand using this technique. In addition, the use of high-voltage capacitors increases system costs.

The proposed MG, consisting of a qZS-ES-CHBMLI, avoids the use of a DC/DC converter and increases efficiency. With the proposed EMS, it is not necessary to redistribute the power from the healthy phases to the faulty phase, because the single-phase control system balances the power within each phase using the BESSs according to its SOC. This allows an increase in the operating range of the MG and improves its reliability against multiple faults. Furthermore, because it is not necessary to increase the voltage at the output of the converter, acceptable levels of overmodulation are maintained, which means that the THD remains stable before and after the occurrence of faults.

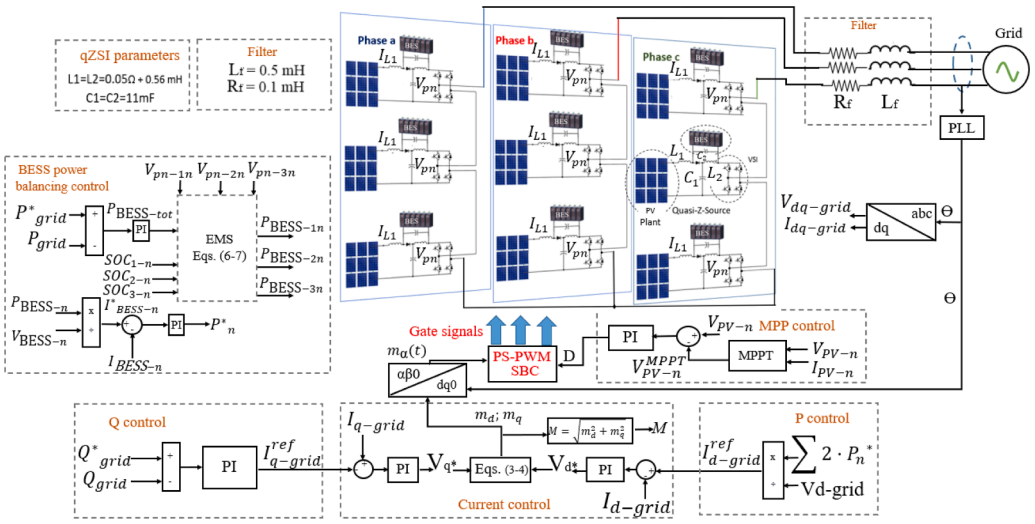

(a)

(b)

Fig. 1. a) Configuration and control scheme of the MG under study. b) SOC proportional EMS flowchart.

1.5. Motivation

Few studies have addressed the multi-fault issue for a three-phase ES-CHBMLI with a PV power generation-based MG. The post-fault control configurations are focused on neutral-point-shifted by adding a FZS, incrementing the converter output voltage and overmodulating [14]. Having the ability to tolerate a wider range of faults is advantageous in order to reduce the time when the converter is not functioning. However, there are drawbacks to increasing the voltage at the DC level. For instance, electrolytic capacitors and switching devices with higher voltage ratings are required, resulting in increased cost. Additionally, the same configuration of the PV generator will require a higher voltage-boost ratio for the DC/DC conversion stage, which typically leads to greater power loss during normal operation. In this work, a qZS-CHBMLI topology is presented to avoid these drawbacks, as there is no need for DC/DC converters.

In PV applications, it is unlikely for the undamaged bridges to provide the same amount of power. When it comes to large-scale PV farms covering vast areas, it is expected that power generation will be uneven owing to variations in the solar irradiance and module temperatures throughout the farm. The imbalance power problem is typically solved by balancing the SOCs, allowing the BESSs to act as a single unit [24]. This work introduces a new EMS that aims to balance the uneven power distribution in each phase during a converter fault or different PV power production. By using this technique, the DC voltage remains stable, avoiding overmodulation. Additionally, the operational capacity of the MG is expanded, due to the ability of the BESSs to handle multiple fault scenarios.

1.6. Contributions

According to the commented above, the main contributions of this work are the following:

1) Development of a decoupled control system for a three-phase grid-connected MG with PV power plants, BESSs and qZS-CHBMLI to deliver renewable clean energy to the utility grid.
2) Multi-fault tolerant operational control scheme of the ES-qZS-CHBMLI under unequal power generation. When one bridge faults it is bypassed, and the remaining healthy bridges in each phase equilibrate the unbalanced power. The design of a novel EMS based on SOC proportional distribution allows to perform a phase-to-phase power balance system under multi-fault issues, different irradiances and several changes in the power demand of the system operator without overmodulation.
3) Experimental hardware in the loop (HIL) verification for the proposed three-phase ES-qZS-CHBMLI with a PV power generation-

Table 1
BESS parameters.

Symbol	Parameter	Value
$V_{BESS-A} = V_{BESS-B} = V_{BESS-C}$	Rated voltage (V)	60
$P_{BESS-A} = P_{BESS-B} = P_{BESS-C}$	Rated power (W)	2618
$Q_{BESS-A} = Q_{BESS-B} = Q_{BESS-C}$	Rated capacity (Ah)	43.63
SOC_{1A}	SOC of BESS 1-A (%)	80
SOC_{2A}	SOC of BESS 2-A (%)	60
SOC_{3A}	SOC of BESS 3-A (%)	20
SOC_{1B}	SOC of BESS 1-B (%)	80
SOC_{2B}	SOC of BESS 2-B (%)	65
SOC_{3B}	SOC of BESS 3-B (%)	90.1
SOC_{1C}	SOC of BESS 1-A (%)	35
SOC_{2C}	SOC of BESS 2-A (%)	80
SOC_{3C}	SOC of BESS 3-A (%)	14.95

based MG. The MG runs in an OPAL4510 unit whereas the control system is implemented in a dSPACE MicroLabBox prototype.

1.7. Organization of the paper

After the introduction, the MG under study is explained in Section II and the proposed fault-tolerant control scheme and the EMS are detailed in Section III. Section IV validates the operation of the MG under multi-fault scenarios through MATLAB/Simulink and experimental results. Finally, the conclusions of this paper are drawn in Section V.

2. Microgrid under study

Fig. 1 illustrates the topology of the three-phase ES-qZS-CHBMLI photovoltaic grid-connected MG. Each phase is composed of three individual modules and each module consists of a PV power generator, VSI, q-impedance network and BESS. Finally, the MG is connected to the local grid through a R-L filter. Table 1 collects the main BESSs parameters. The impedance network parameters are the same for each converter, as shown in Fig. 1.

A seven-level ES-qZS-CHBMLI and a PV power plant of 14.4 kW compose each phase. The layout of each individual PV power generator consists of 2 modules connected in series and 6 strings, thus is 12 panels of 400 W. The system has a base power of $P_B = 4.8$ kW and the rated voltage of the utility grid is 380 V line-to-line. The temperature of each PV panel is considerate constant at 25 ºC. The DC output of the qZS is connected to a VSI and the three VSI are connected in series in each phase to arrange a qZS-CHBMLI configuration. The modular configuration of the CHBMLI allows the achievement of the maximum power point in the PV power plant as well as the regulation of the power injected simultaneously.

The selected BESS is a Li-Ion battery connected in parallel with the capacitor C_{2-n} in the impedance network. The impedance network is composed of two inductors (L_{1-n}, L_{2-n}), two capacitors (C_{1-n}, C_{2-n}) and a diode (see Fig. 1). The qZS configuration involves two configurations: (a) The traditional Non-Shoot-Through state (NST), where the legs of the inverter are connected or disconnected, and (b) The Shoot-Through (ST) state, where two switches in the same column are activated at the same time [4]. The steady-state operation of the qZSI has been deeply studied in the literature [35].

The voltage boost ability (B) of the qZSI can be controlled through the duration of the Shoot-Through state (D), where v_{pn} is the output voltage of the impedance network and v_{pv} is the output voltage of the PV generator. V_{C1-n} is the voltage across the capacitor C1-n, $i_{L1-n}$and i_{L2-n} are the inductor currents, and P_{PV} is the PV power.

Each H-bridge of the CHB has three different levels: +Vpn, -Vpn and zero. To coordinate the different voltage levels, a phase-shift pulse width modulation (PS-PWM) was adopted. Furthermore, Simple Boost Control (SBC) was considered in this study to control the ST states. The ST states are defined according to the upper (V_p) and the lower limits (V_n) of SBC. PS-PWM is an extension of traditional PWM. In this scenario, a modified unipolar sinusoidal pulse-width modulation (SPWM) strategy is utilized for each module. This involves comparing the reference modulating signal from the converter control with a triangular carrier to generate switching signals for the positive half-cycle (ranging from 0 to +Vpn). Additionally, a second modulating signal, phased-shifted 180º from the previous, is responsible for generating the switching signals for the negative half-cycle (ranging from 0 to -Vpn). By phase shifting the PWM signals, the harmonics from different phases do not overlap, resulting in a lower THD and improved power quality. A phase shift is introduced in the carriers of the adjoining blocks, causing a shifted switching pattern between the two. In this case, a phase shift of 180/k (k being the number of converters per phase, i.e. 3) has been used to reduce the harmonics at the output of the system.

The multilevel output voltage is obtained through a phase shifted between the triangular (carrier) signals. In this way, the switching signal for the NST state are obtained, whereas the SBC is applied for the ST states. Additional operational details of the SBC can be found in [36]. In this study, each CHB is a seven-level converter.

Finally, a RL filter has been employed to smooth out the current delivered to the main grid. The filter resistance (R_f) and filter inductance (L_f) have been selected as $R_f = 0.1m\Omega$ and $L_f = 0.5m\Omega$, respectively, according to the procedure described in [37,38].

3. Microgrid control system

Fig. 1 depicts the control scheme. It is composed of three independent modules: (1) MPPT control, to the PV system extracts the maximum power from the sun, (2) EMS to balance the MG under multi-fault scenarios and unequal power generation, and (3) decoupled control to track the power requirements. Two independent variables were used to attain effective control. The Shoot-Through duty cycle (D_n) is responsible for the MPPT of the PV panels and the modulation index (M_n) is employed to perform the decoupled control of P and Q.

3.1. Energy management system for power balancing control

The target of the EMS is to equilibrate the unbalanced power generation of the MG due to multi-fault issues and unequal PV power generation. Fig. 1b shows the EMS structure. It performs a proportional power sharing distribution based on the BESS SOC. Two different constraints are implemented for the safe operation of the BESSs. First, there are two SOC thresholds denoted as SOC_{low} and SOC_{high}, which cannot be exceeded. Furthermore, the maximum power that each BESS will be able to manage in discharging or charging mode (P^{max}_{BESS-n}) cannot overcome the BESS rated power (P^{rated}_{BESS}). Based on these premises, the BESS power can be calculated as follows [34]:

$$P^{dischar}_{BESS-n} = \frac{P_{\mathrm{BESS}-tot} \cdot SOC_n}{\sum SOC_n} \; P^{char}_{BESS-n} = \frac{P_{\mathrm{BESS}-tot} \cdot DOD_n}{\sum DOD_n} \tag{1}$$

where $P_{\mathrm{BESS}-tot}$ denotes the total BESS power for each phase, $P^{dischar}_{BESS-n}$is the BESS power in discharging mode and P^{char}_{BESS-n} is the BESS power in charging mode.

In the case of the power delivered by the photovoltaic panels is lower than the grid requirement ($P_{\mathrm{PVn}-tot} < P^{*}_{grid-\ n}$) the BESSs work in discharging mode. Analogously, when the PV power plants generate more power than demanded; ($P_{\mathrm{PVn}-tot} > P^{*}_{grid-\ n}$), the BESSs work in charging mode. If both powers are equal, the BESSs power is set to zero. According to Fig. 1b, there are four different operation modes for the proposed EMS:

1. Safe mode: In the case of $SOC_{low} < SOC_n < SOC_{high}$, all BESS will operate in safe mode and according to the power balance between

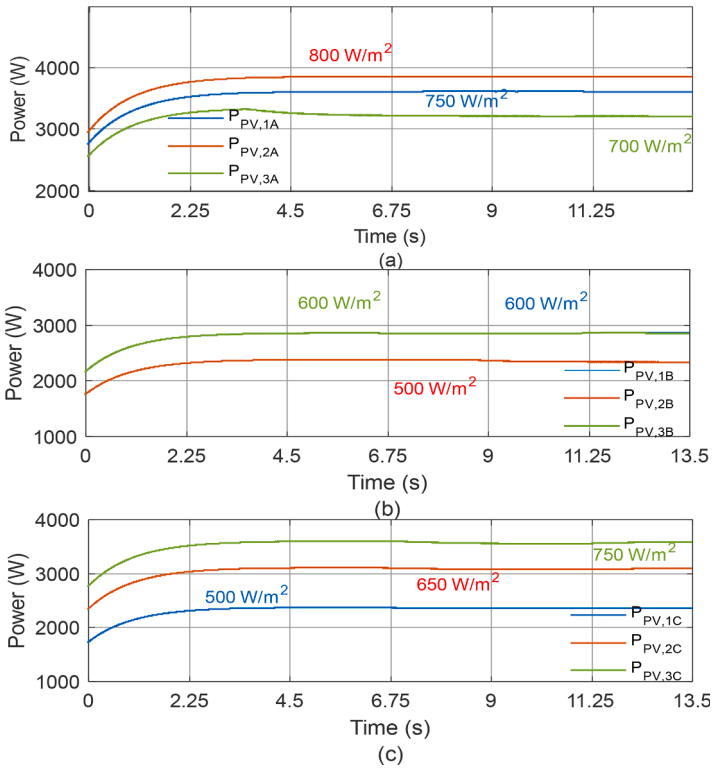

Fig. 2. PV Power: (a) PFV phase a, (b) PFV phase b and (c) PFV phase c.

$P_{\mathrm{PVn}-tot}$ and $P^{*}_{grid-\ n}$. The BESSs power are distributed following Eq. (1).

2. High SOCs mode: In charging mode, if one BESS fulfills the inequation $SOC_n \geq SOC_{high}$ that BESS cannot be charged more. Therefore, that BESS power is set to zero, and the remaining BESS are charged until they reach $SOC_{i,j} \geq SOC_{high}$.
3. Low SOCs mode: If $SOC_n \leq SOC_{low}$ and $P_{\mathrm{PVn}-tot} < P^{*}_{grid-\ n}$, that BESS power is set to zero. Similarly, the remaining active BESSs are discharged until they reach $SOC_{i,j} \leq SOC_{low}$.
4. Bridge fault mode: When one bridge fault occurs, it is bypassed and therefore, the voltage of that module is zero ($V_{pn-n} = 0$). The remaining BESSs continue charging or discharging to equilibrate the power balance.

Note that subscript "n" refers to any one BESS within any one phase, and the subscripts "i,j" refer to the other two BESSs in the same phase.

3.2. Power grid control

The power grid control of the three-phase MG is managed with an independent single-phase control (the same for each phase). The d-q frame is adopted to implement the control scheme. The phase angle (Θ) between the grid voltage and grid current was computed using a phase-locked loop (PLL). The grid voltage (V_{grid}) and current (I_{grid}) are measured and transformed to d-q frame. This transformation is achieved by first expressing the sinusoidal components of V_{grid} and I_{grid} in orthogonal stationary real-imaginary variables, α and β, respectively. The imaginary component (β) is delayed ¼ period to the real component (α) and then the transformation α-β frame to d-q frame is computed with the phase angle Θ.

The DC power at the VSI (P^{*}_{n}) is calculated with a PI controller which adjusts the BESS reference current (I^{*}_{BESS-n}) obtained by the EMS to track the BESS measured current ($I_{\mathrm{BESS}-n}$).

Two independent current loops are implemented to address the P and Q control. For P control, owing to the series connection of the H-bridge, the grid current injected to the grid is [35]:

$$I^{*}_{d-grid} = \frac{2 \cdot P^{tot}_{grid-n}}{V_{d-grid}} = \frac{2 \cdot \sum P^{*}_{n}}{V_{d-grid}} \tag{2}$$

where V_{d-grid} is the direct component of the grid voltage and P^{tot}_{grid-n} is the total power that each phase injects into the grid.

The direct component of the measured current (I_{d-grid}) is adjusted using a PI controller, which modifies the direct component of the grid voltage (V_{d-grid}). Eq. (3) calculates the direct component of the modulation index (m_{d-n}) for a PS-PWM modulation technique [35]:

$$m_{d-n} = \frac{2 \cdot a_{n-P} \cdot V_{d-grid}}{V_{pn-n}} \quad a_{n-P} = \frac{P^{*}_{n}}{P^{tot}_{grid-n}} = \frac{P^{*}_{n}}{\sum P^{*}_{n}} \tag{3}$$

where $a_{n,P}$ is a distribution factor that represents the percentage of active power delivered by each module.

In the case of Q control, a PI controller adjusts the reference quadratic component of the grid current (I^{*}_{q-grid}) to track the reference power (Q^{*}_{grid}). The same scheme control for P is applied to Q, according to the following expressions [34]:

$$m_{q-n} = \frac{2 \cdot a_{n-Q} \cdot V_{q-grid}}{V_{pn-n}} \quad a_{n-Q} = \frac{Q^{*}_{n}}{Q^{tot}_{grid-n}} = \frac{Q^{*}_{n}}{\sum Q^{*}_{n}} \tag{4}$$

where $a_{n,Q}$ is a distribution factor that represents the percentage of active power delivered by each module. The total reactive power is calculated according to Eq. (4).

The PS-PWM SBC block computes the switching signals for the VSIs of the multilevel inverter. The direct and quadrature components of the modulation index are transformed to α-β frame. The real component of the modulation index ($m_{\alpha-n}$) is compared with the triangular carrier signal to obtain the switching signals for the VSIs of the multilevel inverter. The ST states are defined according to the upper (V_p) and the lower limit (V_n) of the SBC. The upper limit of the SBC modulation is selected as $V_P = 1 - D_n$, and the lower as $\mathrm{V}n = D_n - 1$.

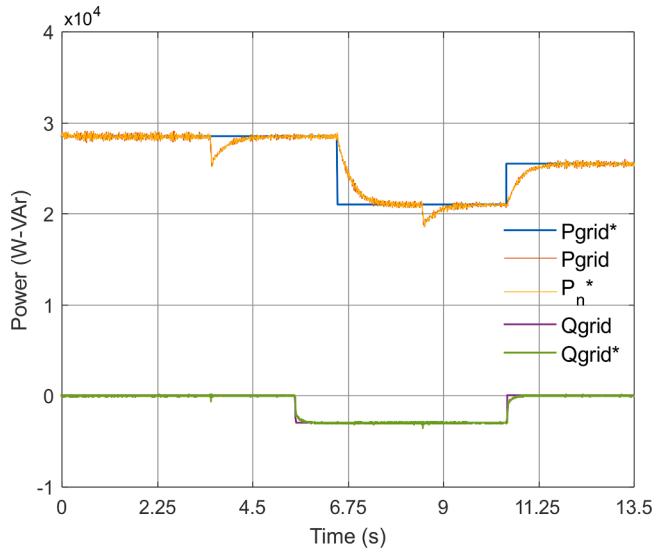

Fig. 3. Active and reactive powers delivered to the grid.

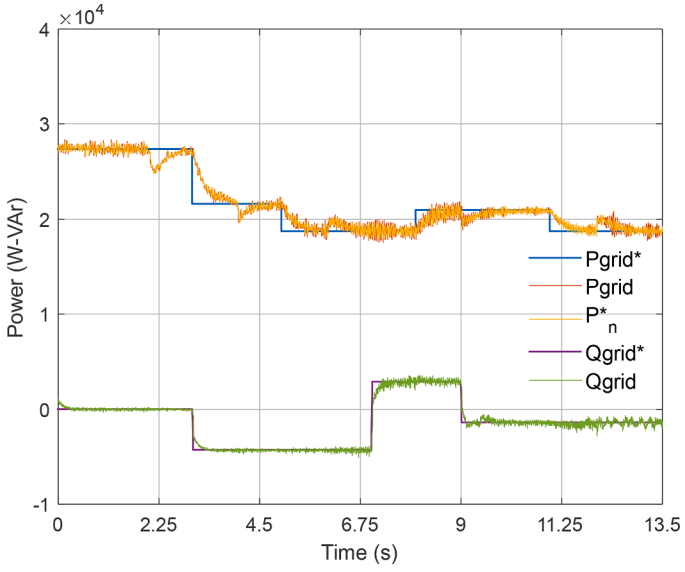

Fig. 4. Active and reactive powers delivered to the grid considering different weather conditions, load variations and multi-faults.

3.3. Maximum power point tracking

The MPPT subsystem receives the PV voltage (V_{PV-n}) and the PV current (I_{PV-n}) to compute the maximum power point voltage (V^*_{PV-n}) for each operation condition. The Perturb & Observe (P&O) algorithm is employed to achieve the MPPT strategy. The P&O algorithm works perturbing (changing) the operating voltage or current of the PV system and observing the resulting changes in the output power. Based on this observation, the algorithm determines the direction in which the operating point needs to be adjusted to achieve the maximum power point (MPP). In the implemented algorithm, the perturbation is caused by increasing or decreasing the PV voltage.

The P&O algorithm starts setting an initial operating point for the PV system, specifically at 95.8 V, which corresponds to the MPP for an incident solar radiation of 1000 W/m^2. The algorithm perturbs the operating point with small incremental changes on the control parameter, which, in this case, is the PV voltage. After the perturbation, the output power of the PV system is measured. This measurement is then compared with the previous. If the output power increases, then the algorithm continues to perturb in the same direction. If the power decreases, the algorithm reverses the direction of the perturbation. This sequence of perturbations and observations is repeated continuously. Once the algorithm converges to the MPP, it maintains the operating point at that level to maximize the power output, ensuring that the PV system operates optimally.

A PI controller adjusts D_n in order to V_{PV-n}tracks V^*_{PV-n}. D_n is not only applied to perform the MPPT, also the PV voltage is boosted according. The maximum production regardless of sun irradiation is ensured according to the individual MPPT for each PV generator.

4. Results and discussion

This section discusses the fault-tolerant control method under several conditions. Thus, multi-fault scenarios, different irradiation conditions and different grid power requirements are considered and studied. In this sense, this section is organized as follows: the power grid fault-tolerant operation is described in Section 4.1; the EMS for power balancing control is detailed in Section 4.2; the overmodulation control results are shown in Section 4.3; the sensitivity analysis is performed in Section 4.4 and finally, a Hardware-in-the-loop (HIL) real time test is represented in Section 4.5.

4.1. Power grid fault-tolerant control

This subsection assesses the validity of fault monitoring and EMS for the proposed MG under normal conditions and failure scenarios. First, a detailed simulation with constant irradiation was performed. Then, a simulation considering weather changes and grid power variations was conducted to validate the proposed control scheme under different operating conditions.

Fig. 2 depicts the PV power under different irradiation conditions for the nine PV power plants. Different productions in PV power generators should lead to the injection of unbalanced grid currents. The proposed control scheme allows equilibration of unbalanced phase-to-phase power, as discussed below.

The reactive and active powers, and the total DC power at VSI input (P^*_n) injected to the grid is represented in Fig. 3. From 0 to 3.5 s, the MG operates under normal conditions. Each PV power generator generates the MPP whereas the EMS equilibrates the power in each phase to deliver balanced three-phase grid currents. The grid active power reference (P^*_{grid}) is set to 27.36 kW and the grid reactive power reference (Q^*_{grid}) takes a value of 0 VAr (unity power factor). At 3.5 s, the third bridge of phase "a" (bridge 3-a) faults and it is bypassed. The EMS detects this situation and the remaining healthy bridges of phase "a" compensate the power loss. At 5.5 s, the system operator changes $Q^*_{grid} = -2.88\ KVAr$ p.u and at 6.5 s P^*_{grid} is decreased to 20.16 kW. At 8.5 s, a new fault is produced at the second bridge of phase "b" (bridge 2-b) and it is bypassed. To ensure the grid power requirements, the EMS sends new power references to the remaining healthy bridges in phase "b". Finally, at 10.5 s, the system operator changes P^*_{grid} to 24.48 kW and Q^*_{grid} backs to 0 VAr.

The control of P and Q in a scenario of changing irradiation and power demands from the system operator is illustrated in Fig. 4. Table 2 displays the weather changes and the variations in the reference power. Furthermore, a fault in converter 3a is considered at $t = 4$ s, and a fault in converter 2b at $t = 9$ s. As seen, the proposed control system is able to manage the variations of load and PV power while ensuring the control of the power delivered to the utility grid.

Furthermore, a sensitivity analysis has been carried out in Section 4.4 to show the performance of the proposed MG under random input variables. This study consists of 200 different scenarios of P and Q, where the appropriate response of the proposed control scheme can be observed.

Table 2
Irradiation changes and P-Q variation.

Irradiance (W/m^2)	Irradiance change	Irradiance (W/m^2)	Irradiance change	Irradiance (W/m^2)	Irradiance change
$I_{FV,1A}$	750 to 500 ($t = 2$ s)	$I_{FV,2A}$	600 to 800 ($t = 6$ s)	$I_{FV,3A}$	500 to 700 ($t = 12$ s)
$I_{FV,1B}$	800 to 600 ($t = 2$ s)	$I_{FV,2B}$	500 to 400 ($t = 6$ s)	$I_{FV,3B}$	650 to 800 ($t = 12$ s)
$I_{FV,1C}$	700 to 500 ($t = 2$ s)	$I_{FV,2C}$	600 to 900 ($t = 6$ s)	$I_{FV,3C}$	750 to 850 ($t = 12$ s)
P^*_{grid}(W)		P^*_{grid} change	$Q^*_{grid}(VAr)$	Q^*_{grid} change	
27,360		21,600 ($t = 3$ s)	0	-4320 ($t = 3$ s)	
21,600		18,720 ($t = 5$ s)	-4320	2880 ($t = 7$ s)	
18,720		20,880 ($t = 8$ s)	2880	-1440 ($t = 9$ s)	
20,880		18,720 ($t = 3$ s)	-1440	-1440	

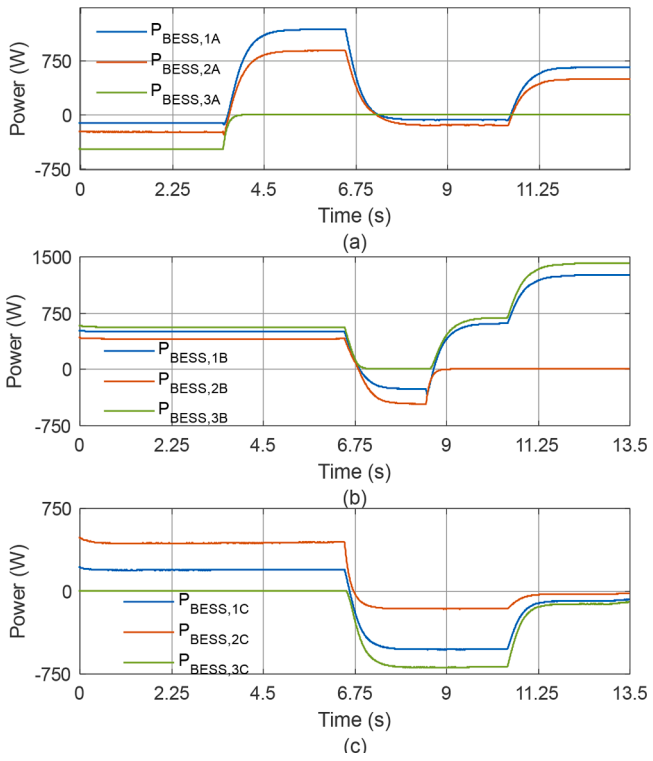

Fig. 5. BESS power: (a) BESS phase a, (b) BESS phase b and (c) BESS phase c.

4.2. Energy management system for power balancing control

This section describes the operation of the proposed EMS to balance the power injected into the local grid under multiple faults, different irradiances and grid power references. The BESSs power are represented in Fig. 5. The proposed EMS allows an independent control scheme for each phase, maintaining SOC between $SOC_{high} = 90$ % and $SOC_{low} = 15$ % and limiting the maximum BESS power to its rated power. In the case of phase "a" (Fig. 5a), the BESSs operate in a safe mode because the SOC of all BESSs are within the thresholds. The total PV power in each phase is defined as the sum of the individual power modules ($P^{tot}_{PV,n} = \sum P_{PV,n}$). Due to $P^{tot}_{PV,A} > P^*_{grid}$ from 0 to 3.5 s, the BESSs are charged according to the EMS discussed in Section 3. At 3.5 s, bridge 3a faults and $BESS_{3A}$ sets its power to 0. The remaining bridges of phase "a" change from charging to discharging mode to fulfill the grid demands. At 6.5 s, the system operator decreases P^*_{grid}, and therefore, the BESSs return to charging mode. Finally, at 10.5, an increment in P^*_{grid}implies that the BESSs start to discharge.

For phase "b" (Fig. 5b), $SOC_{3B} > SOC_{high}$and this BESS cannot be charged further. From 0 to 6.5 s, all BESSs are operating in discharging mode according to the power balance. At 6.5 s, the reduction in P^*_{grid}changes the operating mode of the BESS from discharging to charging. $BESS_{3B}$sets its power to 0 and the remaining BESSs in phase "b" start charging. At 8.5 s, the fault produced at bridge 2b changes the operation from charging to discharging mode, setting $P_{BESS,2B} = 0$ and back to discharging mode for $BESS_{3B}$. Finally, phase "c" (Fig. 5c) presents the case of $SOC_{3C} < SOC_{low}$ and this BESS cannot be discharged further. From 0 to 6.5 s, $P_{BESS,3C} = 0$ and the remaining BESSs are discharged. When the system operator decreases P^*_{grid} at 6.5 s, all the BESSs

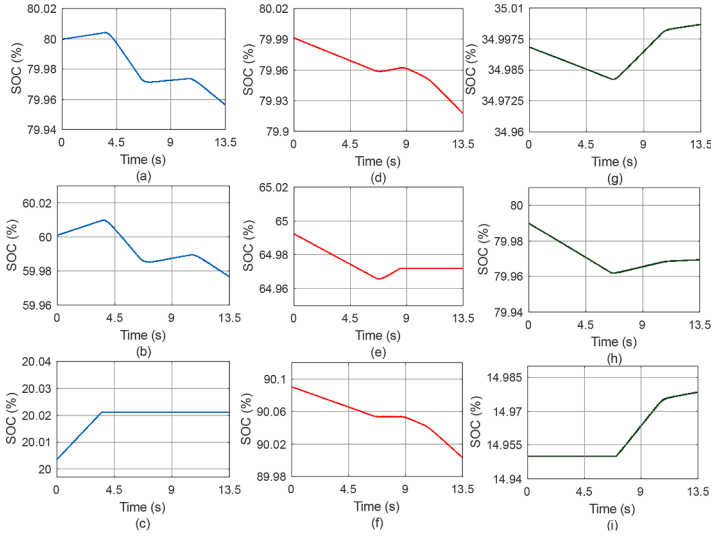

Fig. 6. SOC levels (a) SOC 1A, (b) SOC 2A, (c) SOC 3A, (d) SOC 1B, (e) SOC 2B, (f) SOC 3B, (g) SOC 1C, (h) SOC 2C, (i) SOC 3C.

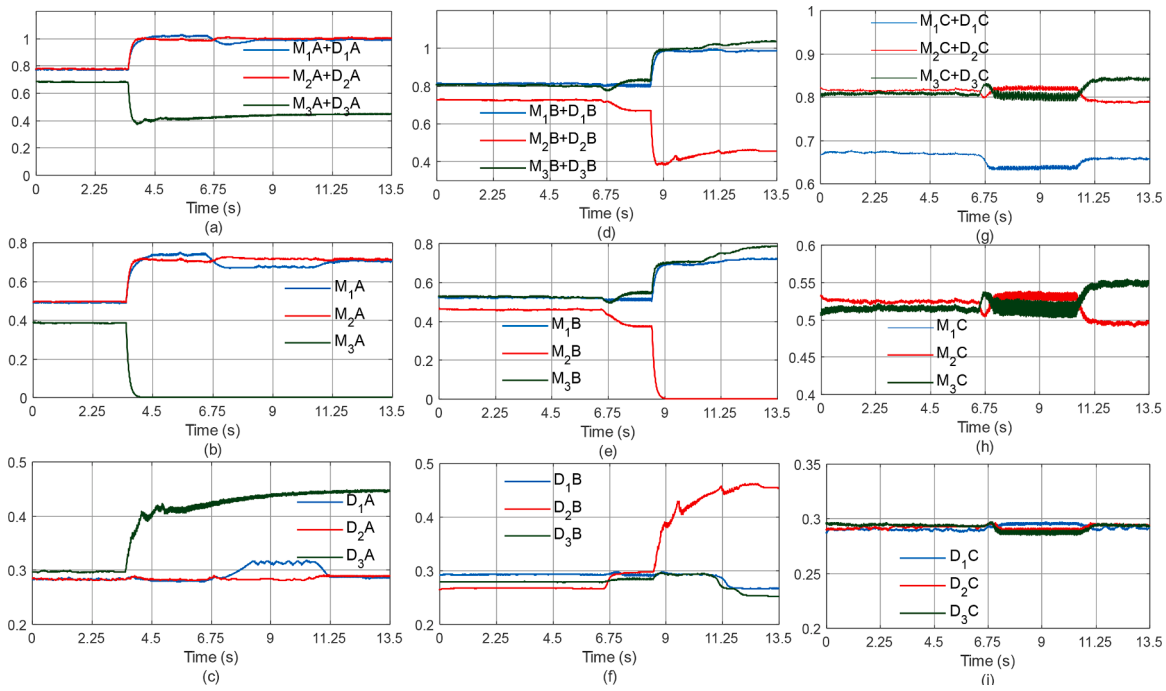

Fig. 7. Shoot-through (D) and Modulation index(M): (a) $M + D$ phase a, (b) M phase a, (c) D phase a, (d) $M + D$ phase b, (e) M phase b, (f) D phase b, (g) $M + D$ phase c, (h) M phase c, (i) D phase c.

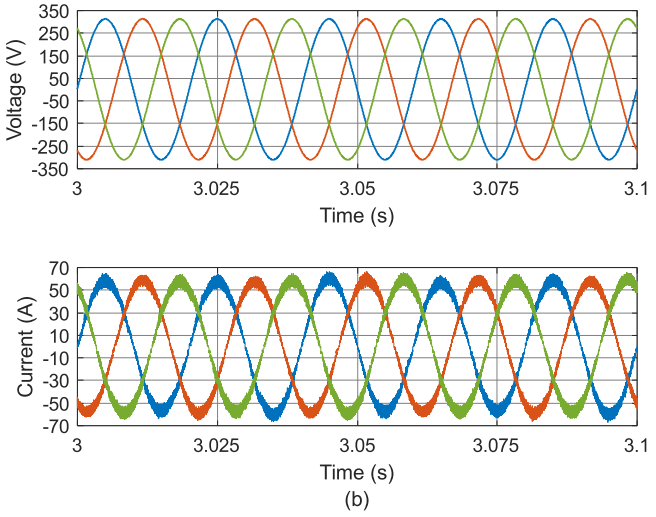

Fig. 8. (a) Grid voltage and (b) grid current under normal operation.

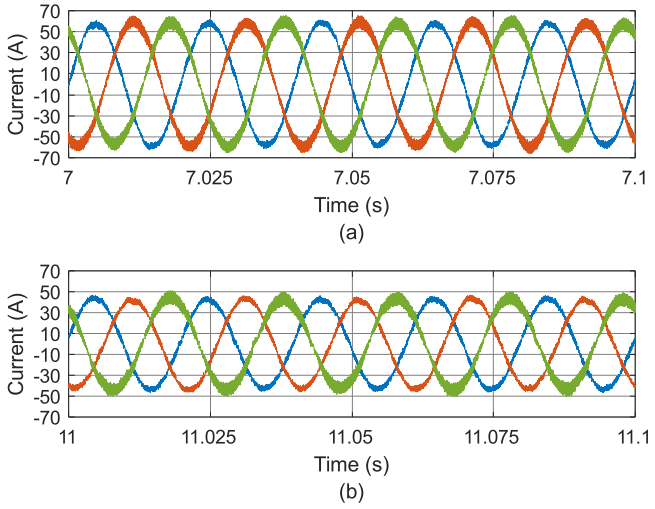

Fig. 9. (a) Grid current under fault in converter 3-a, and (b) Grid current under fault in converter 2-b.

operate in charging mode and they remain charging until the end of the simulation.

Fig. 6 denotes the SOC levels for phase "a", "b" and "c" respectively. The BESSs operating under safe mode are represented in Figs. 6a–c, where all the BESSs operate according Eq (1). When a fault occurs in bridge 3a, $BESS_{3A}$ does not inject or save any power, and thus SOC_{3A}remains constant after a fault at 3.5 s, as denoted Fig. 6c. Fig. 6f depicts the SOC operating when $SOC_{3B} > SOC_{high}$ and therefore, $BESS_{3B}$cannot be charged from 6.5 s to 8.5 s. In addition, when a fault is produced in $BESS_{2B}$ at 8.5 s, that bridge is bypassed (Fig. 6e) and the remaining bridges change to discharging mode as illustrate Fig. 6d and f.

Finally, the operating mode when $SOC_{3C} < SOC_{low}$ is represented in Fig. 6i. From 0 to 6.5 s, SOC_{3C} remains constant because $BESS_{3C}$ cannot be discharged. At 6.5 s, the system operator decreases P^{*}_{grid} and the BESSs change to charging mode until the remainder of the simulation (Fig. 6g and h). It is noteworthy that the charging and discharging dynamics are conditioned by the SOC value. In discharging mode, the BESSs with a higher SOC are discharged faster and in charging mode, those BESSs with a lower SOC are charged faster. The results show the effectiveness of the proposed fault-tolerant control, as well as the strength of the EMS

Table 3
THD analysis of three phase grid current.

Parameter	Normal condition	Failure scenario 1	Failure scenario 2
THD_{I-A}(%)	5.62	3.95	4.59
THD_{I-B}(%)	5.19	6.82	4.80
THD_{I-C}(%)	5.59	6.40	8.40
Mean	5.59	5.72	5.93

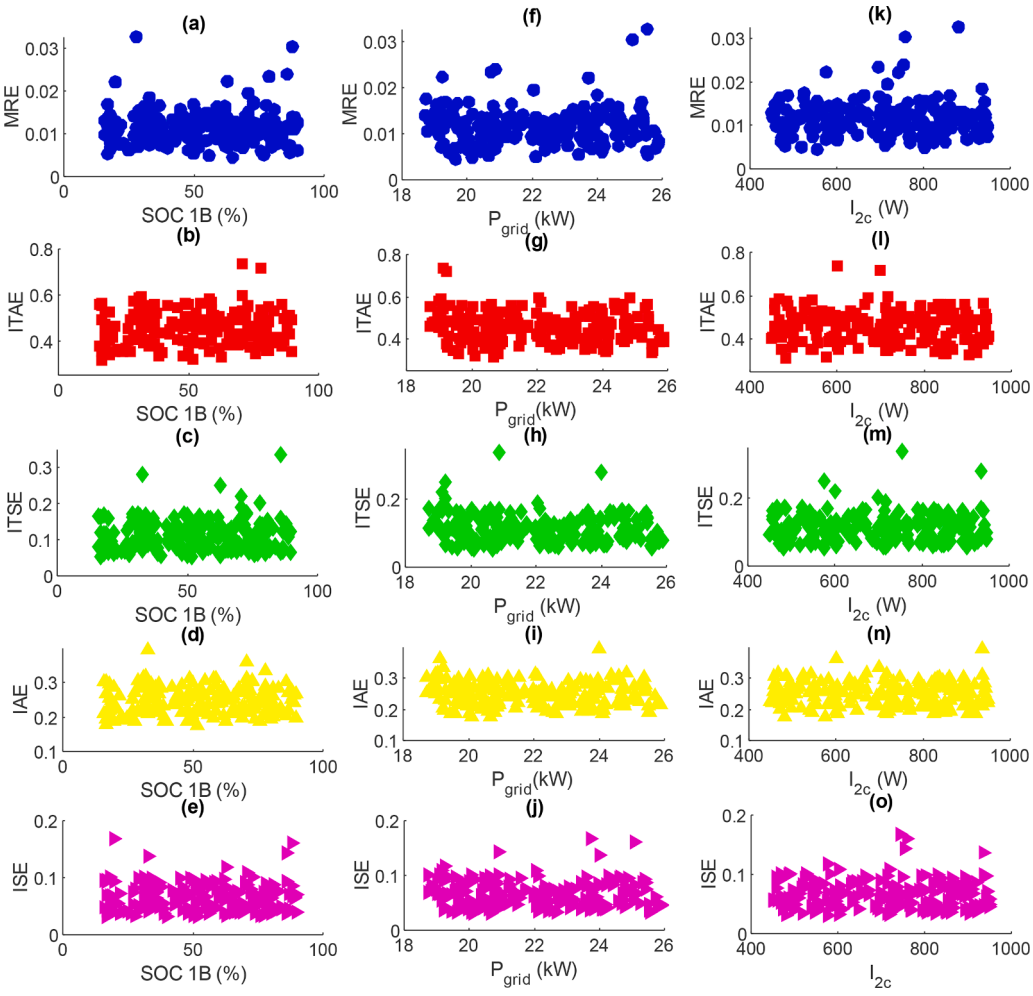

Fig. 10. Sensitivity analysis of P_{grid}. (a) MRE versus SOC 1-b. (b) ITAE versus SOC 1-b. (c) ITSE versus SOC 1-b. (d) IAE versus SOC 1-b. (e) ISE versus SOC 1-b. (f) MRE versus P_{grid}.(g) ITAE versus P_{grid}. (h) ITSE versus P_{grid}. (i) IAE versus I_{2c}. (j) ISE versus P_{grid}. (k) MRE versus I_{2c}. (l) ITAE versus I_{2c}. (m) ITSE versus I_{2c}. (n) IAE versus I_{2c}. (o) ISE versus I_{2c}.

under multi-fault scenarios and unequal power generation. The three-phase grid current are balanced and the system operator demands are fulfilled.

4.3. Overmodulation control

To avoid overmodulation, authors in [39] proposed that the shoot-through duty cycle (D) adds with the modulation index (M) should be less than one, thus $D_n + M_n \leq 1$. In this section, the results of M and D are shown in Fig. 7. Fig. 7a–c represent the values of D_{nA}, M_{nA} and the sum of D_{nA} and M_{nA} for phase "a". It can be seen that after a fault, $M_{1A}$and M_{2A} increase their values (Fig. 7b) but the sum of $D_{1A} + M_{1A}$ and $D_{2A} + M_{2A}$is still less than one (Fig. 7a). After a fault, at 3.5 s, M_{3A}takes a value of 0. The values of D_{nB}, M_{nB} and the sum of D_{nB} and M_{nB} for phase "b" are represented in Fig. 7d–f. At 8.5, M_{2B} is equal to 0 (Fig. 7e) and the sum of $D_{1B} + M_{1B}$ and $D_{3B} + M_{3B}$ (Fig. 7d) does not exceed unity although M_{1B} and M_{3B} are increased. Fig. 7g-i represent the values of D_{nC}, M_{nC} and the sum of D_{nC} and M_{nC} for phase "c". Phase "c" operates under normal conditions, and therefore, the values of M_{1C},$M_{2C}$and M_{3C} (Fig. 6h) as well as the sum of $D_{nC} + M_{nC}$ (Fig. 7g) remain without overmodulation.

Fig. 8 depicts the grid phase-to-ground pick voltage (Fig. 8a) and grid current (Fig. 8b) under normal operation and unity power factor. The post-fault operation of the grid current is represented in Fig. 9, where it can be seen that the MG delivers to the local grid a balanced three-phase current after a multi-fault scenario.

To perform a numerical analysis of the reliability of the system, the THD has been calculated. Table 3 collects the mean value of the THD for the three-phase grid currents. As seen, the mean THD increases 2.3 % after one fault and 3.7 % after two faults. These results are consistent with those obtained in Fig.7, where the addition of M and D was lower than 1, demonstrating the proper overmodulation control of the proposed multi-fault-tolerant control and a low THD increment after multi-fault issues.

4.4. Sensitivity analysis

To strengthen the validation of the proposed multi-fault-tolerant control, a sensitivity and stability analysis has been performed. The study consists of 200 simulations, each one lasting 3 s, where the most significant inputs of the system are modified randomly. In these simulations, the key input parameters of the control system, such as the initial BESS SOC, irradiance, and grid active and reactive power references, are modified to observe the control results and the overall system response. The MG under study is composed of nine BESSs, nine PV power plants and there are two grid references, namely P^*_{grid} and Q^*_{grid}. This results in a total of 20 input variables. To represent a

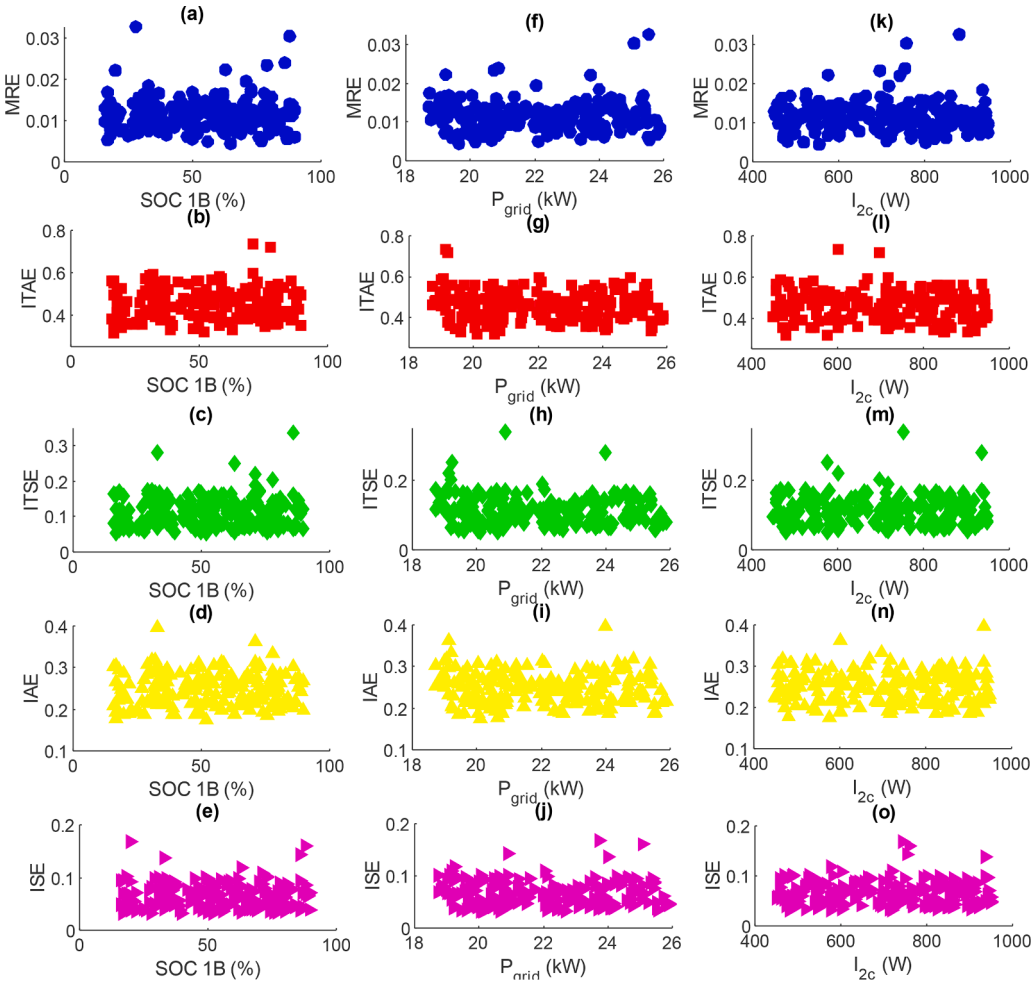

Fig. 11. Sensitivity analysis of Q_{grid}. (a) MRE versus SOC 1-b. (b) ITAE versus SOC 1-b. (c) ITSE versus SOC 1-b. (d) IAE versus SOC 1-b. (e) ISE versus SOC 1-b. (f) MRE versus P_{grid}.(g) ITAE versus P_{grid}. (h) ITSE versus P_{grid}. (i) IAE versus I_{2c}. (j) ISE versus P_{grid}. (k) MRE versus I_{2c}. (l) ITAE versus I_{2c}. (m) ITSE versus I_{2c}. (n) IAE versus I_{2c}. (o) ISE versus I_{2c}.

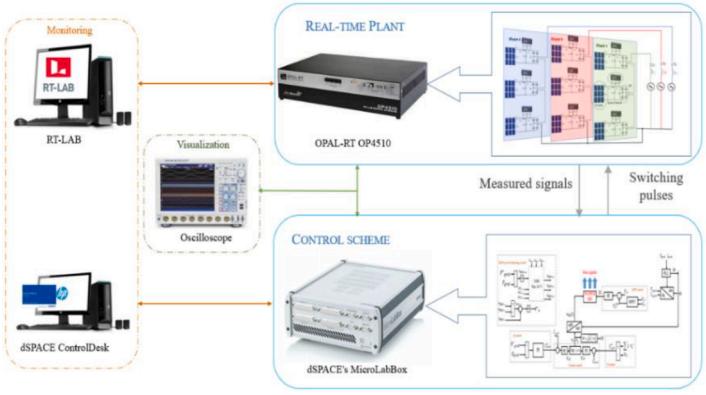

Fig. 12. Experimental setup implemented in the laboratory.

scenario that compromises the main components of the MG, a random BESS and a random PV power plant are selected to analyze the case study.

The outputs of the sensitivity and stability analysis considered in the evaluation of the control system are five performance indices: the Mean Relative Error (MRE), Integral Time Absolute Error (ITAE), Integral Time Square Error (ITSE), Integral Absolute Error (IAE), and Integral Square Error (ISE). These performance indices should be close to zero to ensure appropriate control. Among the different indices, the optimal value depends on the application of the study. In this study, the ITAE was chosen as a reference index because it provides accurate results. All the aforementioned indices are calculated and included in this study. The results obtained from the sensitivity analysis are shown in Figs. 10 and 11.

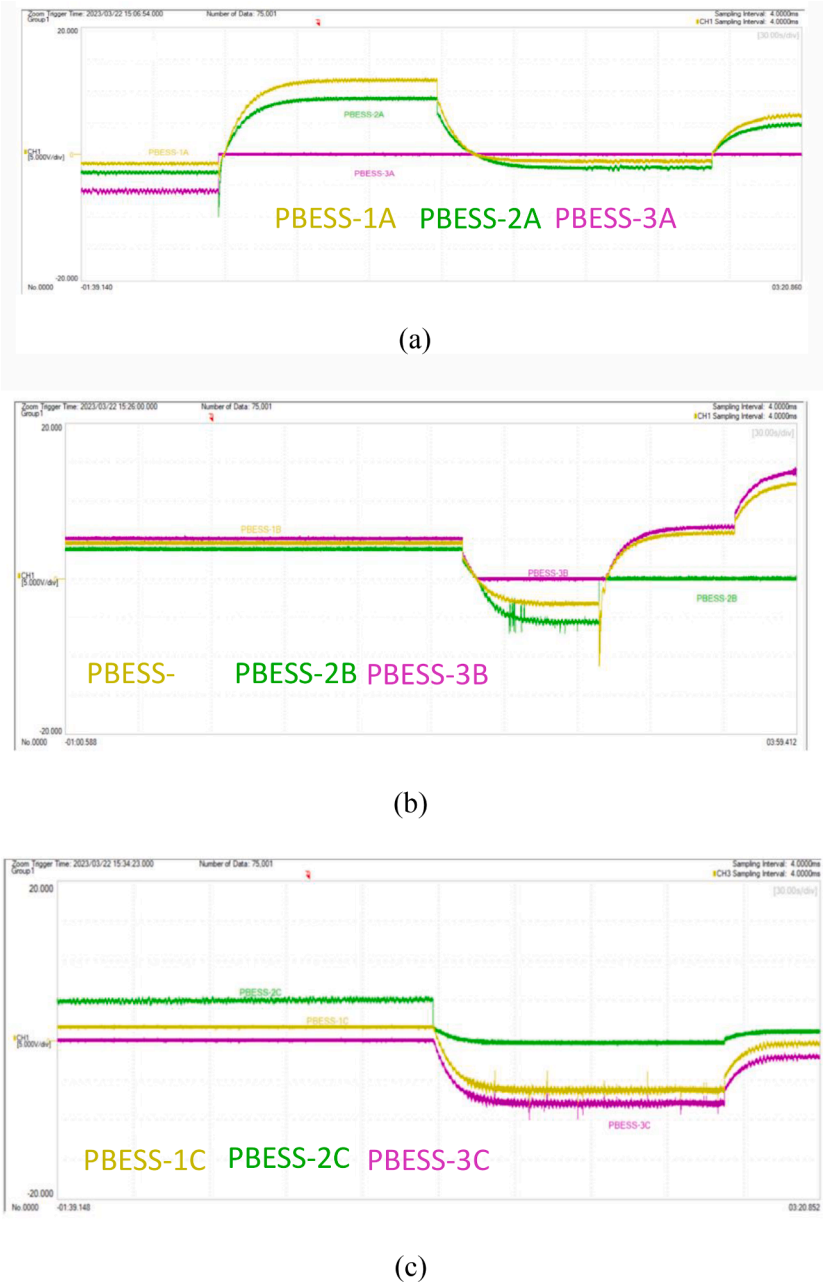

Fig. 13. Experimental results measured with the Yokogawa DLM4018 oscilloscope. (a) BESS power in phase-a, (b) BESS power in phase-b, and (c) BESS power in phase-c.

The sensitivity analysis of P_{grid} is shown in Fig. 10. It can be observed that all the performance indices remain consistently close to the same values. Irrespective of the considered scenario, the grid active power remained stable and maintained the desired value. This behavior evidences the adequate response of the system to the randomly generated inputs. The SOC 1-b is randomly generated within a range of 15 % to 90 % (as shown in Fig. 10(a–e)), the grid active power varies from 18.7 kW to 25.9 kW (as shown in Fig. 10 (f–j)), and the irradiance of the PV power plant two of phase (I2-c) can take a value between 450 W/m^2 and 950 W/m^2 (Fig. 10(k–o)). In Fig. 11, the performance indices of Q_{grid} are represented against randomly generated inputs. The results indicate a consistent distribution of the control indices throughout the simulations, demonstrating the reliability of the system.

4.5. Hardware in the Loop (HIL) verification

To perform an experimental validation, the proposed fault-tolerant control scheme and EMS, a Hardware in the Loop (HIL) test is described in this section. Fig. 12 represents the real-time hardware setup to test the multi-fault control system. The power system runs in real-time in an OPAL-RT-4510 unit. OPAL is a HIL simulator that allows implementing and testing computational models developed in MATLAB/Simulink in real time. It is specifically designed to be programmed using RT-LAB software. The output range of the analogue signals is ±16 V. The high performance of the four cores allows editing, building, loading, executing, and monitoring the model in a realistic and controlled environment. The control system is implemented in a dSPACE MicroLabBox unit, which is programmed using Simulink. The dSPACE MicroLabBox is a compact and versatile hardware unit designed for rapid control prototyping and testing of control algorithms. It is equipped with a powerful

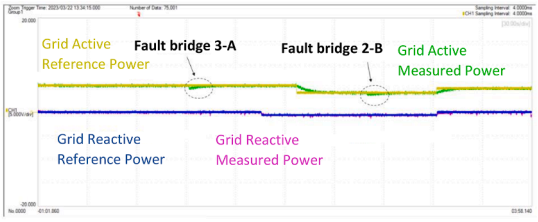

(a)

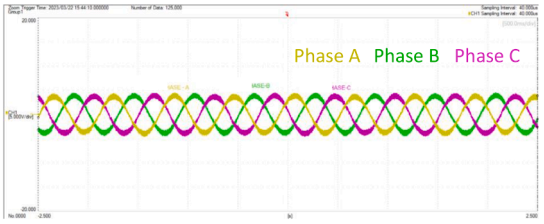

(b)

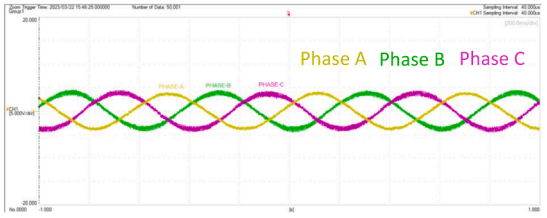

(c)

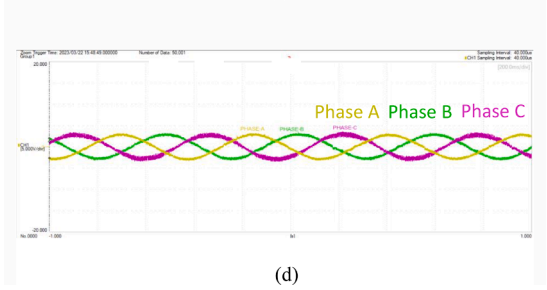

(d)

Fig. 14. Yokogawa DLM4018 oscilloscope measurements. (a) Active and reactive power, (b) Three-phase grid current under normal operation, (c) Three-phase grid current under fault in converter 3-A and, (d) Three-phase grid current under fault in converter 2-B.

dual-core processor, FPGA and a high range of I/O interfaces, with analogue signals in the range of ±10 V. A Yokogawa DLM4038 oscilloscope is employed to visualize the real-time simulation. The Yokogawa DLM4038 is a digital storage oscilloscope designed for precise waveform analysis. It offers a bandwidth of 350 MHz, a maximum sample rate of 2.5 GS/s and a memory depth of up to 250 Mpoints per channel. The BESSs power are represented in Fig. 13a–c. The range of these signals is set as −20 V and +20 V on a scale of 5 V/div. The proposed EMS respond appropriately to fulfill the system operator references, limiting the BESSs power according to the SOC thresholds and bridge faults.

Fig. 14a represents the correct response of the control system under variable power requirements and remains stable under multi-fault scenarios. The active reference and measured power are represented with the yellow and green signals, respectively, while the reactive reference and measured power are represented by blue and purple signals, respectively. The range of the grid powers is set as −20 V and +20 V at a scale of 5 V/div. The three-phase grid balanced currents are illustrated in Fig. 14b, which it can be seen the operation under normal conditions and unequal PV generation. The simulation results verify the simulation performed. The post-fault grid currents are represented in Fig. 14 c and d respectively. The range of these signals is set as −20 V and +20 V on a scale of 5 V/div. It is depicted that the system is able to recover the control after multi-fault issues, and deliver to the local grid a balanced three-phase current.

The experimental results are consistent with those obtained in Sections 4.1, 4.2, 4.3 and 4.4 in MATLAB/Simulink and validate the performance of the control system proposed in this work, balancing the power system and increasing the reliability of renewable grid-connected technologies.

5. Conclusions

In this paper, a multi-fault tolerant operation of an ES-qZS-CHBMLI with PV generators-based MG was presented to increase the reliability of Distributed Energy Resources. The contributions of this paper are: (1) Development of a decoupled power control system for a three-phase grid-connected MG with PV power plants, BESSs and qZS-CHBMLI, ensuring the grid power requirements; (2) Design of multi-fault tolerant control which is able to equilibrate the unbalanced problem under different power generated by the PV generator and bridge faults. When one bridge faults, it is bypassed and the remaining healthy bridges compensate for lack of power in the microgrid. The single-phase control allows an individual control for each phase, balancing the power according to the EMS. Therefore, a multi-fault scenario in different phases can be addressed to maintain the balance of the utility grid; (3) Design of a new EMS to coordinate the BESSs power exchanges. The proposed EMS based on SOC performs a proportional sharing power algorithm between BESS, and thus, BESSs with higher SOC are discharger deeper and the same time, and BESSs with lower SOC are more charged. These results were verified with experimental HIL tests for a three-phase ES-qZS-CHBMLI with a PV generation-based MG.

Therefore, an equilibrate three-phase current system is injected even under multi-fault scenarios in different phases. The results achieved with MATLAB simulation and them with an OPALRT4510 unit and dSPACE MicroLabBox prototyping guarantee the correct operation of the fault-control scheme under different issues and irradiance conditions. The THD analysis revealed a 2.3 % increase in the average injected three-phase current after the first fault, and a 3.7 % increase after the second fault. The sensitivity analysis showed that the error in the control of P and Q was very low in 200 simulations, with the ITAE remaining between 0.3 and 0.6. These findings confirm the reliability of the proposed multi-fault tolerant MG. Future research could explore a hybrid renewable generation system that combines PV with wind turbines and other types of ESSs, such as ultracapacitors, to evaluate the effectiveness of the proposed control algorithm.

CRediT authorship contribution statement

Pablo Horrillo-Quintero: Conceptualization, Formal analysis, Investigation, Methodology, Writing – original draft. **Pablo García-Triviño:** Conceptualization, Formal analysis, Investigation, Methodology, Writing – original draft. **Raúl Sarrias-Mena:** Conceptualization, Formal analysis, Investigation, Methodology, Writing – original draft. **Carlos A. García-Vázquez:** Formal analysis, Methodology, Writing – original draft. **Luis M. Fernández-Ramírez:** Conceptualization, Funding acquisition, Methodology, Project administration, Supervision, Writing – review & editing.

Declaration of Competing Interest

The authors declare that they have no known competing financial interests or personal relationships that could have appeared to influence the work reported in this paper.

Data Availability

Data will be made available on request.

Acknowledgments

This work was partially supported by the Regional Ministry of Economic Transformation, Industry, Knowledge, and Universities of Junta de Andalucía (under Grant PY20_00317), and Ministerio de Ciencia e Innovación, Agencia Estatal de Investigación, FEDER, UE (Grant PID2021-123633OB-C32 supported by MCIN/AEI/10.13039/501100011033/ FEDER, UE).

References

[1] "GLOBAL MARKET OUTLOOK, " 2014. [Online]. Available online in https://helapco.gr/wpcontent/uploads/EPIA_Global_Market_Outlook_for_Photovoltaics_2014-2018_Medium_Res.pdf.
[2] "Statistical Review of World Energy 2022." [Online]. Available online in https://www.bp.com/content/dam/bp/businesssites/en/global/corporate/pdfs/energy-economics/statistical-review/bp-stats-review-2022-full-report.pdf.
[3] S. Kouro, J.I. Leon, D. Vinnikov, L.G. Franquelo, Grid-connected photovoltaic systems: an overview of recent research and emerging PV converter technology, IEEE Ind. Electron. Mag. 9 (2015) 47–61, https://doi.org/10.1109/MIE.2014.2376976.
[4] Y. Liu, H. Abu-Rub, B. Ge, F. Blaabjerg, O. Ellaban, P. Chiang, Impedance Source Power Electronic Converters, John Wiley and Sons-IEEE Press, Chichester, UK, 2016.
[5] H. Hatas, M.N. Almali, Design and control of a novel topology for multilevel inverters using high frequency link, Electr. Power Syst. Res. 221 (2023), https://doi.org/10.1016/j.epsr.2023.109458.
[6] H. Hatas, M.N. Almali, Design and control of bypass diode multilevel inverter using a single DC source, Electr. Power Syst. Res. 216 (2023), https://doi.org/10.1016/j.epsr.2022.109039.
[7] E. Kabalcı, Multilevel Inverters: Introduction and Emergent Topologies, Elsevier, 2021, https://doi.org/10.1016/B978-0-12-821668-2.09991-8.
[8] S. Jayaprakash, R. Balamurugan, S. Gopinath, T. Kokilavani, S. Maheswaran, 3-Phase multi-inverter with cascaded H-bridge inverter designing and implementation for renewable system, Sustain. Energy Technol. Assess. 52 (2022), https://doi.org/10.1016/j.seta.2022.102088.
[9] J. Stöttner, C. Hanzl, C. Endisch, Extensive investigation of symmetrical and asymmetrical cascaded multilevel inverters for electric vehicle applications, Electr. Power Syst. Res. 209 (2022), https://doi.org/10.1016/j.epsr.2022.108009.
[10] Y. Yu, G. Konstantinou, B. Hredzak, V.G. Agelidis, Operation of cascaded H-bridge multilevel converters for large-scale photovoltaic power plants under bridge failures, IEEE Trans. Ind. Electron. 62 (2015) 7228–7236, https://doi.org/10.1109/TIE.2015.2434995.
[11] W. Song, A.Q. Huang, Fault-tolerant design and control strategy for cascaded H-bridge multilevel converter-based STATCOM, IEEE Trans. Ind. Electron. 57 (2010) 2700–2708, https://doi.org/10.1109/TIE.2009.2036019.
[12] E. Villanueva, P. Correa, J. Rodriguez, M. Pacas, Control of a single-phase cascaded H-bridge multilevel inverter for grid-connected photovoltaic systems, IEEE Trans. Ind. Electron. 56 (2009) 4399–4406, https://doi.org/10.1109/TIE.2009.2029579.
[13] S. Rivera, B. Wu, S. Kouro, H. Wang, D. Zhang, Cascaded H-bridge multilevel converter topology and three-phase balance control for large scale photovoltaic systems, in: Proceedings - 2012 3rd IEEE International Symposium on Power Electronics for Distributed Generation Systems, PEDG 2012, 2012, pp. 690–697, https://doi.org/10.1109/PEDG.2012.6254077.
[14] Y. Yu, G. Konstantinou, C.D. Townsend, V.G. Agelidis, Comparison of zero-sequence injection methods in cascaded H-bridge multilevel converters for large-scale photovoltaic integration, IET Renew. Power Gener. 11 (2017) 603–613, https://doi.org/10.1049/iet-rpg.2016.0621.
[15] Y. Yu, G. Konstantinou, B. Hredzak, V.G. Agelidis, Power balance optimization of cascaded H-bridge multilevel converters for large-scale photovoltaic integration, IEEE Trans. Power Electron. 31 (2016) 1108–1120, https://doi.org/10.1109/TPEL.2015.2407884.
[16] R. Jami, J. Nakka, S.V.K. Pulavarthi, Grid integration of three phase solar powered fault-tolerant cascaded H-bridge inverter, Int. J. Circuit Theory Appl. 50 (2022) 2566–2583, https://doi.org/10.1002/cta.3272.
[17] P. Lezana, G. Ortiz, Extended operation of cascade multicell converters under fault condition, IEEE Trans. Ind. Electron. 56 (2009) 2697–2703, https://doi.org/10.1109/TIE.2009.2019771.
[18] S. Ouni, M.R. Zolghadri, M. Khodabandeh, M. Shahbazi, J. Rodríguez, H. Oraee, et al., Improvement of post-fault performance of a cascaded H-bridge multilevel inverter, IEEE Trans. Ind. Electron. 64 (2017) 2779–2788, https://doi.org/10.1109/TIE.2016.2632058.
[19] V. Sridhar, S. Umashankar, A comprehensive review on CHB MLI based PV inverter and feasibility study of CHB MLI based PV-STATCOM, Renew. Sustain. Energy Rev. 78 (2017) 138–156, https://doi.org/10.1016/j.rser.2017.04.111.
[20] R. Choupan, S. Golshannavaz, D. Nazarpour, M. Barmala, A new structure for multilevel inverters with fault-tolerant capability against open circuit faults, Electr. Power Syst. Res. 168 (2019) 105–116, https://doi.org/10.1016/j.epsr.2018.11.013.
[21] A.A. Stonier, B. Lehman, An intelligent-based fault-tolerant system for solar-fed cascaded multilevel inverters, IEEE Trans. Energy Convers. 33 (2018) 1047–1057, https://doi.org/10.1109/TEC.2017.2786299.
[22] B. Ge, H. Abu-Rub, F.Z. Peng, Q. Lei, A.T. De Almeida, F.J.T.E. Ferreira, et al., An energy-stored quasi-Z-source inverter for application to photovoltaic power system, IEEE Trans. Ind. Electron. 60 (2013) 4468–4481, https://doi.org/10.1109/TIE.2012.2217711.
[23] K. Li, K.J. Tseng, Energy efficiency of lithium-ion battery used as energy storage devices in micro-grid, in: IECON 2015 - 41st Annual Conference of the IEEE Industrial Electronics Society, Institute of Electrical and Electronics Engineers Inc., 2015, pp. 5235–5240, https://doi.org/10.1109/IECON.2015.7392923.
[24] L. Maharjan, T. Yamagishi, H. Akagi, J. Asakura, Fault-tolerant operation of a battery-energy-storage system based on a multilevel cascade PWM converter with star configuration, IEEE Trans. Power Electron. 25 (2010) 2386–2396, https://doi.org/10.1109/TPEL.2010.2047407.
[25] K. Kandasamy, M. Vilathgamuwa, K.J. Tseng, Inter-module state-of-charge balancing and fault-tolerant operation of cascaded H-bridge converter using multi-dimensional modulation for electric vehicle application, IET Power Electron. 8 (2015) 1912–1919, https://doi.org/10.1049/iet-pel.2014.0943.
[26] F. Eroglu, A.M. Vural, A critical review on state-of-charge balancing methods in multilevel converter based battery storage systems, in: Proceedings - 2022 IEEE 4th Global Power, Energy and Communication Conference, GPECOM 2022, Institute of Electrical and Electronics Engineers Inc., 2022, pp. 14–19, https://doi.org/10.1109/GPECOM55404.2022.9815810.
[27] G. Liang, G.G. Farivar, S. Ceballos, H.D. Tafti, J. Pou, C.D. Townsend, et al., Unbalanced active power distribution of cascaded multilevel converter-based battery energy storage systems gobble, IEEE Trans. Ind. Electron. 69 (2022) 13022–13032, https://doi.org/10.1109/TIE.2021.3137442.
[28] W. Jiang, C. Zhu, C. Yang, L. Zhang, S. Xue, W. Chen, The active power control of cascaded multilevel converter based hybrid energy storage system, IEEE Trans. Power Electron. 34 (2019) 8241–8253, https://doi.org/10.1109/TPEL.2018.2882450.
[29] J. Yu, Power-matching based SOC balancing method for cascaded H-bridge multilevel inverter, CPSS Trans. Power Electron. Appl. 5 (2020) 352–363, https://doi.org/10.24295/CPSSTPEA.2020.00029.
[30] J. Yu, R. Yu, H. Wen, X. Lin, K. Hu, Simplified SVPWM-based SoC balancing strategy for three-phase cascaded H-bridge multilevel converter in off-grid energy storage systems, Int. J. Electr. Power Energy Syst. 137 (2022), https://doi.org/10.1016/j.ijepes.2021.107474.
[31] P. Franzese, M. Ribera, A. Cervone, D. Iannuzzi, Optimized control strategy for single-phase multilevel cascaded converter in a distributed PV-BESS system, Electr. Power Syst. Res. 214 (2023), https://doi.org/10.1016/j.epsr.2022.108818.
[32] W. Liang, Y. Liu, J. Peng, A day and night operational quasi-Z source multilevel grid-tied PV power system to achieve active and reactive power control, IEEE Trans. Power Electron. 36 (2021) 474–492, https://doi.org/10.1109/TPEL.2020.3000818.
[33] L. de Oliveira-Assis, E.P.P. Soares-Ramos, R. Sarrias-Mena, P. García-Triviño, E. González-Rivera, H. Sánchez-Sainz, et al., Simplified model of battery energy-stored quasi-Z-source inverter-based photovoltaic power plant with Twofold energy management system, Energy 244 (2022), https://doi.org/10.1016/j.energy.2021.122563.
[34] P. Horrillo-Quintero, P. García-Triviño, R. Sarrias-Mena, C.A. García-Vázquez, L. M. Fernández-Ramírez, Model predictive control of a microgrid with energy-stored quasi-Z-source cascaded H-bridge multilevel inverter and PV systems, Appl. Energy 346 (2023), https://doi.org/10.1016/j.apenergy.2023.121390.
[35] D. Sun, B. Ge, F.Z. Peng, A.R. Haitham, D. Bi, Y. Liu, A new grid-connected PV system based on cascaded H-bridge quasi-Z source inverter, in: IEEE International Symposium on Industrial Electronics, 2012, pp. 951–956, https://doi.org/10.1109/ISIE.2012.6237218.
[36] DC/AC Half-Bridge Converter, Voltage-Sourced Converters in Power Systems, John Wiley & Sons, Ltd, 2010, pp. 21–47, https://doi.org/10.1002/9780470551578.ch2.
[37] M. Liserre, F. Blaabjerg, S. Hansen, Design and control of an LCL-filter-based three-phase active rectifier, IEEE Trans. Ind. Appl. 41 (2005) 1281–1291, https://doi.org/10.1109/TIA.2005.853373.
[38] L. de Oliveira-Assis, E.P.P. Soares-Ramos, R. Sarrias-Mena, P. García-Triviño, L. M. Fernández-Ramírez, Large-scale grid connected quasi-Z-source inverter-based PV power plant, in: 2020 IEEE International Conference on Environment and Electrical Engineering and 2020 IEEE Industrial and Commercial Power Systems Europe (EEEIC /I&CPS Europe), Madrid, Spain, 2020, pp. 1–6, https://doi.org/10.1109/EEEIC/ICPSEurope49358.2020.9160529.
[39] S. Rahman, M. Meraj, A. Iqbal, L. Ben-Brahim, Novel voltage balancing algorithm for single-phase cascaded multilevel inverter for post-module failure operation in solar photovoltaic applications, IET Renew. Power Gener. 13 (2019) 427–437, https://doi.org/10.1049/iet-rpg.2018.5483.